









The First Survey of Quiet Sun Features Observed in Hard X-Rays With NuSTAR

Sarah Paterson¹  · Iain G. Hannah¹  ·
Brian W. Grefenstette²  · Hugh
S. Hudson^{1,3}  · Säm Krucker^{3,4}  ·
Lindsay Glesener⁵  · Stephen M. White⁶  ·
David M. Smith⁷ 

© Springer ●●●●

Abstract We present the first survey of quiet Sun features observed in hard X-rays (HXRs), using the the Nuclear Spectroscopic Telescope ARray (NuSTAR), a HXR focusing optics telescope. The recent solar minimum combined with NuSTAR's high sensitivity has presented a unique opportunity to perform the first HXR imaging spectroscopy on a range of features in the quiet Sun. By studying the HXR emission of these features we can detect or constrain the presence of high temperature (>5 MK) or non-thermal sources, to help understand how they relate to larger more energetic solar phenomena, and determine their contribution to heating the solar atmosphere. We report on several features observed in the 28 September 2018 NuSTAR full-disk quiet Sun mosaics, the first of the NuSTAR quiet Sun observing campaigns, which mostly include steady

✉ S. Paterson
s.paterson.5@research.gla.ac.uk

- ¹ School of Physics & Astronomy, University of Glasgow, University Avenue, Glasgow G12 8QQ, UK
- ² Cahill Center for Astrophysics, California Institute of Technology, 1216 East California Boulevard, Pasadena, CA 91125, USA
- ³ Space Sciences Laboratory University of California, Berkeley, CA 94720, USA
- ⁴ University of Applied Sciences and Arts Northwestern Switzerland, 5210 Windisch, Switzerland
- ⁵ School of Physics & Astronomy, University of Minnesota Twin Cities, Minneapolis, MN 55455, USA
- ⁶ Air Force Research Laboratory, Space Vehicles Directorate, Kirtland AFB, NM 87123, USA
- ⁷ Santa Cruz Institute of Particle Physics and Department of Physics, University of California, Santa Cruz, CA 95064, USA

features of X-ray bright points and an emerging flux region which later evolved into an active region, as well as a short-lived jet. We find that the features' HXR spectra are well fitted with isothermal models with temperatures ranging between 2.0–3.2 MK. Combining the NuSTAR data with softer X-ray emission from *Hinode*/XRT and EUV from SDO/AIA we recover the differential emission measures, confirming little significant emission above 4 MK. The NuSTAR HXR spectra allow us to constrain the possible non-thermal emission that would still be consistent with a null HXR detection. We found that for only one of the features (the jet) was there a potential non-thermal upper limit capable of powering the heating observed. However, even here the non-thermal electron distribution had to be very steep (effectively mono-energetic) with a low energy cut-off between 3–4 keV. The higher temperature or non-thermal sources in the typical quiet Sun features found in this September 2018 data are therefore found to be very weak, if present at all.

Keywords: Corona, Quiet; Heating, Coronal; Jets; Spectrum, X-Ray; X-Ray Bursts, Hard

1. Introduction

The study of the hard X-ray (HXR) emission from the quiet Sun could provide insight into the source of the sustained high temperature of the solar corona, termed the coronal heating problem. It was suggested by Parker (1988) that the source of this heating could be a large number of small-scale energy release events, taking place all through the solar cycle. If such events were weaker versions of flares, they would be expected to produce a HXR signature.

One phenomenon that has been linked to coronal heating is coronal bright points (CBPs), small-scale loop structures located in the lower corona, which are observed in EUV and soft X-rays (SXR) (e.g. Madjarska, 2019). These features are observed throughout the solar cycle, including solar minimum, when the Sun is quiet in the absence of active regions and large flares. Bright points have been studied extensively in EUV and SXR. In EUV, these features typically have lifetimes of < 20 hours (Alipour and Safari, 2015; Zhang, Kundu, and White, 2001), whereas they have been found to be shorter-lived in SXR, with lifetimes of ~ 12 hours (Harvey *et al.*, 1993). These features sometimes have associated transient phenomena, such as “microflares” (Golub *et al.*, 1974; Shimojo and Shibata, 1999), and small-scale eruptions (Mou *et al.*, 2018).

Previous studies have used EUV and SXR observations to investigate the temperatures of bright points. Kariyappa *et al.* (2011) used SXR data from the *Hinode* X-ray Telescope (*Hinode*/XRT) (Kosugi *et al.*, 2007) to study a number of bright points, using filter ratios to determine that their temperatures ranged between 1.1–3.4 MK. Another study by Doschek *et al.* (2010) used EUV data from the *Hinode* Extreme Ultra-violet Imaging Spectrometer, finding that the bright points reached maximum temperatures between 2–3 MK. Alexander, Del Zanna, and Maclean (2011) studied the evolution of a single bright point, using both SXR and EUV data. This study found that throughout the 13 hours of observation, the bright point was almost isothermal, with an average temperature

of 1.3 MK. The Hinode/XRT time profile for this bright point showed a steady increase in intensity for the first two hours of observation, followed by several spikes (which the authors speculated were likely due to heating or reconnection events) until it began to decay.

Bright points can result from bipolar flux emergence. When this process occurs, new magnetic flux emerges to create an emerging flux region (EFR), which may subsequently evolve into a small-scale bright point, an example of which was investigated by Kontogiannis *et al.* (2020). This study tracked the evolution in Hinode/XRT of a bright point associated with an EFR, finding that the bright point exhibited a continuous increase in emission for ~ 1.5 hours before it began to fade. However, rather than a bright point, an EFR may instead evolve into a large-scale active region if the emergence continues (van Driel-Gesztelyi and Green, 2015).

HXR observations of bright points have been made difficult by the faintness of this emission from these sources, and the lack of a solar dedicated instrument able to observe them individually. Previous HXR studies of the quiet Sun (Hannah *et al.*, 2007, 2010) have been performed using data from the *Reuven Ramaty High-Energy Solar Spectroscopic Imager* (RHESSI) (Lin *et al.*, 2002). However, as RHESSI was designed for the observation of bright sources, such as large flare events, only upper limits on the HXR emission from the whole solar disk were obtained. The authors noted that using a sensitive HXR focusing telescope would allow a more detailed study of the energy release mechanisms occurring in quiet Sun features. A more recent paper by Buitrago-Casas *et al.* (2022) also constrains the quiet Sun HXR emission in the 5–10 keV range using data from the *Focusing Optics X-ray Solar Imager* (FOXSI) sounding rocket. This study found similar upper limits to Hannah *et al.* (2010), though using only minutes' worth of data, compared to the days that were required with RHESSI.

The *Nuclear Spectroscopic Telescope Array* (NuSTAR) (Harrison *et al.*, 2013) is a HXR focusing telescope which is capable of being pointed at the Sun to provide sensitive observations of faint solar sources (Grefenstette *et al.*, 2016). Since 2014, there have been a number of NuSTAR solar observing campaigns¹. Much of the work on the NuSTAR solar observations has focused on active region microflares (Wright *et al.*, 2017; Glesener *et al.*, 2017; Hannah *et al.*, 2019; Cooper *et al.*, 2020; Duncan *et al.*, 2021; Cooper *et al.*, 2021), with Glesener *et al.* (2020) reporting for the first time on non-thermal emission detected in a microflare observed with NuSTAR. Kuhar *et al.* (2017) presented work on quiet Sun flares observed by NuSTAR outside of an active region, finding that their temperatures ranged from 3.2–4.1 MK.

NuSTAR has two focal plane modules (FPMA and FPMB), both with a FOV of $12' \times 12'$ (Harrison *et al.*, 2013). Each of these focal plane modules has a 2×2 array of CdZnTe detectors. When observing the Sun it has been used in two modes: dwells, where the same region is observed over the course of one or several NuSTAR orbits (each with ~ 1 hour in sunlight); and full-disk mosaics, where the pointing is continually changed over the course of an orbit to build up an image of the entire disk.

¹Summary of NuSTAR solar observations can be found at https://ianan.github.io/nsigh_all/

NuSTAR’s use of focusing optics means that it can directly image very faint HXR sources on the quiet Sun, and perform spectroscopy on regions of interest. During the recent solar minimum between cycles 24 and 25 (2018–2020), when the solar disk was free of active regions, NuSTAR was used to observe the Sun on a number of occasions, providing several bright points and other quiet Sun phenomena to study. The recent solar minimum combined with NuSTAR’s sensitivity has provided a unique opportunity to study the HXR emission from these features and investigate their contribution to the heating of the solar atmosphere by searching for the presence of a high temperature ($>5\text{MK}$) or non-thermal component due to the presence of accelerated electrons.

Here, we present the first survey of small features in the quiet Sun observed in HXRs with NuSTAR. We present analysis of several features from the 28 September 2018 full-disk mosaics, the first of the NuSTAR quiet Sun observations, including the first HXR imaging spectroscopy of such features. We include in our analysis EUV data from the *Solar Dynamics Observatory’s* Atmospheric Imaging Assembly (SDO/AIA) (Lemen *et al.*, 2012) and SXR data from Hinode/XRT. An overview of this observation is presented in section 2, including NuSTAR spectral fits for several of the observed quiet Sun features and a calculation of NuSTAR non-thermal upper limits for a small jet. More detailed analysis, including NuSTAR spectral fits, differential emission measures, and non-thermal upper limits, for an EFR which later went on to become an active region can be found in section 3. Section 4 details similar analysis for two bright points from this observation.

2. Overview of Observation

On 28 September 2018, NuSTAR observed the quiet Sun for two orbits (18:25–19:25 UT and 20:01–21:01 UT), producing a full-disk mosaic for each. The NuSTAR mosaics, formed over an orbit with \sim an hour in sunlight, are comprised of 25 pointings of duration ~ 100 s which form a 5×5 pattern. The first pointing, P1, is in the top left corner, with the subsequent pointings shifting to the right until P5. P6 is shifted down from P5, with the following four pointings being increasingly shifted to the left. This pattern continues until P25, which is in the bottom right corner of the mosaic. The pointings overlap with each other such that a feature on the disk can be captured up to four times within a single orbit.

For the times of these two orbits, there is also full-disk data available from SDO/AIA and Hinode/XRT (though there is a gap in the data from Hinode/XRT between 19:13–19:38 UT). The NuSTAR mosaics, and the SDO/AIA 211 Å and Hinode/XRT Be-thin full-disk images from the mid-times of both NuSTAR orbits, are shown in Figure 1. NuSTAR is a photon-counting detector, and the data list the photons’ properties, including time of detection, energy, and position on the detector. These NuSTAR full-disk maps are constructed by correcting each pointing for livetime individually and aligning the NuSTAR image with SDO/AIA, and then summing the corrected counts.

Because of the way in which the mosaic tiles overlap, the disk is sampled more times than the limb (which is captured in only one or two pointings, compared

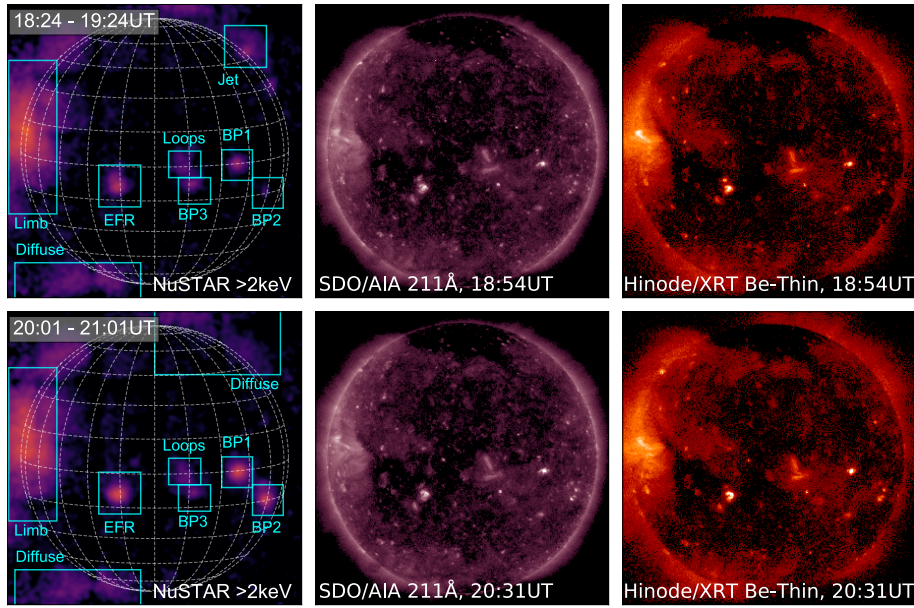


Figure 1. Full disk images for NuSTAR, SDO/AIA 211 Å and Hinode/XRT Be-thin for the two NuSTAR orbits of observation from 28 September 2018. The SDO/AIA and Hinode/XRT images are taken from the mid-times of each of the NuSTAR orbits.

to four pointings on the disk). An additional correction has been applied per detector quadrant to these mosaics to account for this by normalising by the number of times a given region has been sampled over the whole mosaic. Note that these NuSTAR mosaics, as well as all of the NuSTAR images shown here, have been smoothed with a Gaussian filter.

There are several features present in the NuSTAR images, with corresponding sources appearing also in SDO/AIA and Hinode/XRT. In the first NuSTAR orbit but not the second (the NuSTAR images in the top and bottom rows of Figure 1, respectively), there is a faint source that appears in the top right corner of the mosaic, which can be seen to be a jet in SDO/AIA. There is also a set of loops near the centre of the disk, as well as a nearby bright point which is labelled BP3. These two features are captured by NuSTAR in both orbits, and also observed in SDO/AIA 211 Å and Hinode/XRT. Regions of off-disk diffuse emission are also present in NuSTAR. The source that is most striking in the NuSTAR mosaics is the large region of emission from the east limb, which is observed in both NuSTAR orbits. Between the NuSTAR detectors there are chip gaps, and any photons that land on these gaps are not detected. Due to the bright and extended nature of the bright limb emission, these detector gaps are visible crossing through this feature in Figure 1.

One of the most interesting features from this set of mosaics is an EFR which went on to become the NOAA active region 12723 β a few days after this observation. This feature is captured in the mosaics from both orbits, giving the opportunity to study its evolution. Detailed analysis of the EFR can be found in

section 3. Two of the other brightest NuSTAR sources are X-ray bright points, labelled here as BP1 and BP2, which are analysed in section 4.

2.1. Jet

One of the features observed by NuSTAR is the source at the top right of the mosaic in the first panel in Figure 1. This is present in NuSTAR in orbit 1, but not orbit 2, suggesting that it is more short-lived than the other features which appear in both orbits. The mosaic tiles which capture the region that this source lies in are P4, 5, 6, and 7.

SDO/AIA images of this source confirm that it is a compact jet which begins to brighten at around 18:27 UT, and has disappeared by 18:40 UT. SDO/AIA 211 Å and Hinode/XRT Be-thin images from the mid-times of the relevant pointings are plotted in Figure 2, with aligned NuSTAR contours. From the SDO/AIA images, it can be seen that the configuration of this jet is atypical, with the jet material being ejected perpendicularly rather than radially outwards, implying that the overlying magnetic field is pushing it sideways. The lightcurves for this feature are shown in Figure 3. The NuSTAR count rates for each pointing are plotted over the lightcurves for comparison.

Around the time of P4 in Figure 3, during which NuSTAR sees the brightest emission from the jet, there is a peak in both SDO/AIA 211 Å and Hinode/XRT Be-thin. Another peak in SDO/AIA 211 Å coincides with P5, but this feature has decreased in brightness in both NuSTAR and Hinode/XRT. Again showing agreement with Hinode/XRT, though not SDO/AIA 211 Å, the NuSTAR brightness is at its lowest in P6 (making the feature almost indistinguishable from the background), before increasing in brightness in P7. This behaviour is also apparent in the Hinode/XRT images, where the feature appears brighter during the times of NuSTAR P4, 5, and 7 compared to P6. The jet is positioned far enough away from any chip gaps that this change in brightness in NuSTAR is genuine, as opposed to an effect of it moving in and out of detector gaps.

NuSTAR is an imaging spectrometer, allowing the X-ray spectra of these quiet Sun features to be fit to investigate their properties. The spectral fitting of the features presented here was done using XSPEC (Arnaud, 1996), an X-ray spectral fitting program. In order to perform spectral fitting for a given source, a Spectral Response Matrix (SRM) for a circular region enclosing the source is obtained from the Response Matrix and Ancillary Response Files (RMF and ARF) which are generated using the NuSTAR Data Analysis Software. As the features investigated here produce a low number of counts, Cash statistics (Cash, 1979) were used for the fitting, and coronal abundances were assumed.

For this source, and for many of the other quiet Sun features observed with NuSTAR, the HXR emission is faint. Also, although NuSTAR has a high sensitivity, its detector throughput is limited to 400 counts/s/FPM, and the low energy counts dominate. The livetime for these pointings ranges from 67–92 %, though it is ~ 90 % for all pointings barring those that captured the bright region on the east limb. The issues mentioned above combined with the short duration of the mosaic pointing times (~ 100 s) result in noisy spectra that are

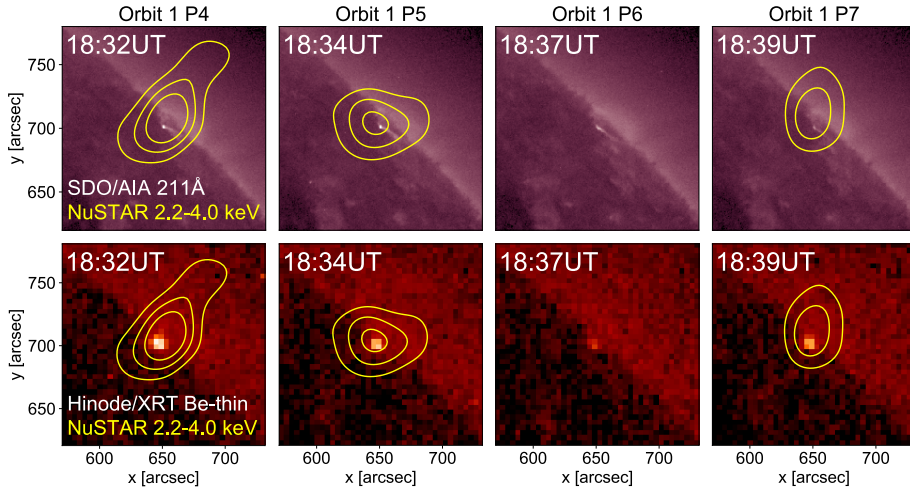


Figure 2. SDO/AIA 211 Å (top) and Hinode/XRT Be-thin (bottom) images of the jet from the mid-times of the four NuSTAR pointings in the first orbit which captured it. Yellow contours represent NuSTAR FPMA + FPMB 2.2–4.0 keV, with the contours aligned with SDO/AIA and plotted at the same levels in all panels ($5, 7, 9 \times 10^{-4}$ counts s^{-1}).

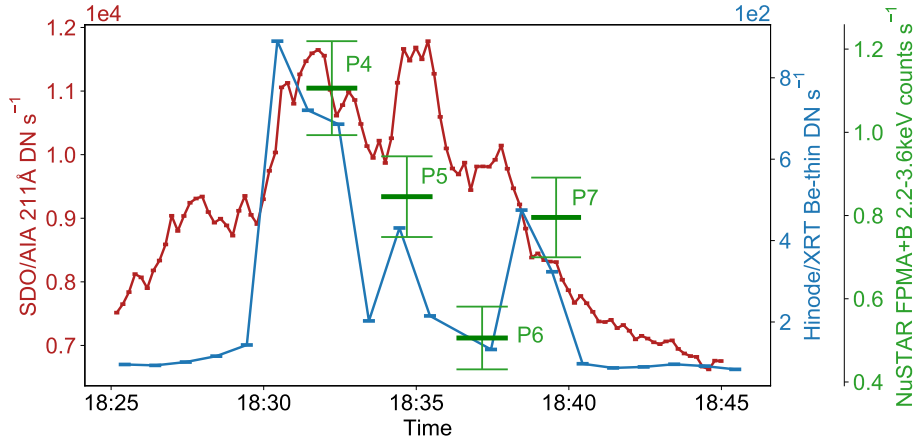


Figure 3. SDO/AIA 211 Å and Hinode/XRT Be-thin lightcurves for the jet. The green lines indicate the NuSTAR FPMA + FPMB livetime-corrected count rates, and their corresponding errors, for the pointings that captured this feature.

generally tricky to fit. This can be improved upon to some extent by simultaneously fitting the FPMA and FPMB spectra for a given source, introducing a multiplicative constant to the fits to account for any systematic difference between the responses of the two telescopes. However, in some cases this is not enough to get good fits for these faint features. Fortunately, this can be further improved by simultaneously fitting the features' spectra from multiple mosaic pointings.

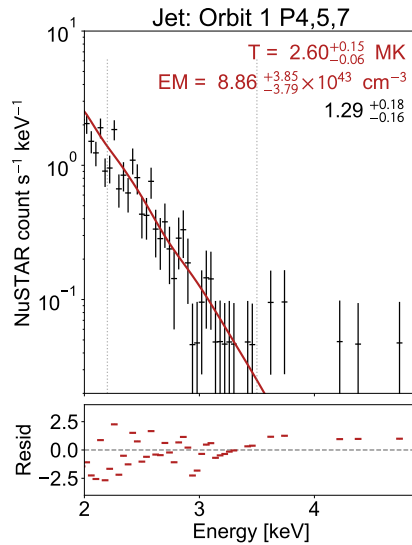


Figure 4. NuSTAR spectral fit for the jet in orbit 1, simultaneously fitting FPMA and FPMB from P4 (18:31:24–18:33:04 UT), 5 (18:33:51–18:35:32 UT), and 7 (18:38:46–18:40:24 UT). Dotted lines indicate fitting range, and temperature and emission measure are marked on the plot. The number in black is the multiplicative constant introduced to account for systematic differences between FPMA and FPMB.

When performing the NuSTAR spectral fitting for this feature, the spectra from P4, 5, and 7 were fit simultaneously. P6 was not used due to the faintness of the NuSTAR emission. A circular region of radius $63''$, and centred on the bright emission, was used for the spectral fitting. Though this source is clearly evolving in SDO/AIA 211\AA , the NuSTAR spectra for each of the pointings were fit individually and it was found that there was no significant change in the temperature or emission measure throughout. Therefore, in order to obtain the best signal-to-noise ratio, the spectra from all three pointings were fit simultaneously with a single thermal APEC model. While it was previously recommended to only fit NuSTAR spectra down to 2.5 keV (Grefenstette *et al.*, 2016), a recent update to NuSTAR’s calibration has now made it possible to fit down to 2.2 keV (Madsen *et al.*, 2021). This is particularly useful in the case of the features studied here, as their spectra do not typically contain many counts above 2.5 keV.

The fit for the NuSTAR jet spectrum, shown in Figure 4, gives a temperature of 2.60 MK and an emission measure of $8.86 \times 10^{43} \text{ cm}^{-3}$. The isothermal model fits the spectrum well, with no indication of a higher temperature component or of any non-thermal emission. This temperature lies in the range of the sensitivity of Hinode/XRT, but lies slightly above the peak in the SDO/AIA 211\AA sensitivity. This may explain the different behaviour of SDO/AIA 211\AA compared to Hinode/XRT and NuSTAR visible in Figure 3.

2.1.1. NuSTAR Non-thermal Upper Limits

The thermal energy of the jet was calculated using the following:

$$E_{th} = 3k_B T \sqrt{EM V} \quad [\text{erg}] \quad (1)$$

where k_B is the Boltzmann constant, V is the volume of the plasma, and T and EM are the temperature and emission measure of the plasma, respectively (Hannah *et al.*, 2008). Note that this equation does not take into account a loop filling factor, which means that this is an upper limit on the thermal energy.

From an SDO/AIA 211 Å image of the jet, it takes up an area of 3'' square. Assuming that the volume is $\sim A^{\frac{3}{2}}$, this gives a volume of $1.04 \times 10^{25} \text{ cm}^3$. Therefore, taking the temperature and emission measure values from the spectrum in Figure 4 ($T = 2.60 \text{ MK}$, $EM = 8.86 \times 10^{43} \text{ cm}^{-3}$), the thermal energy of the jet is $3.26 \times 10^{25} \text{ erg}$.

The calculated thermal energy can be used to obtain a heating requirement for the jet, and combined with information derived from the HXR spectra to determine whether this heating could be non-thermal in nature. The spectrum for the jet was well fit with an isothermal model. However, following the approach of Wright *et al.* (2017), the upper limits of a non-thermal source of accelerated electrons that are still consistent with a null detection can be determined. This was done by adding a non-thermal component to the thermal model determined from the spectral fitting. This thick target non-thermal model depends on three parameters: the power-law index, δ , the low-energy cutoff, E_c , and the total electron flux, N_N . The total power in the distribution is then:

$$P(> E_c) = 1.6 \times 10^{-9} \frac{\delta - 1}{\delta - 2} N_N E_c \quad [\text{erg s}^{-1}] \quad (2)$$

For a range of δ and E_c values, the upper limit on N_N was found such that it was consistent with a null detection. For each N_N value, the thermal model and the model with the additional non-thermal component were both folded through the NuSTAR response, and a synthetic NuSTAR spectrum was generated for each. For each δ and E_c combination, N_N was reduced until the two spectra lay within each others' Poissonian errors between 2 and 4 keV, and there were < 4 counts above 4 keV — consistent with a null detection to 2σ (Gehrels, 1986). The jet spectrum is noisy due to the short integration time and the faintness of the source, and so this upper limit test does not result in exactly the same upper limit being obtained every time. Therefore, for each E_c and δ combination the upper limit on N_N was calculated 1000 times. This produced a distribution which was well fit with a Gaussian, of which the peak location was taken to be the non-thermal upper limit, with the spread indicated by the standard deviation of the distribution. This upper limit on N_N in turn gave a corresponding upper limit on the power on the non-thermal distribution, as plotted in Figure 5. In addition to testing the upper limits for several values of δ , the upper limits were also found for the case of a mono-energetic beam of electrons. In the case of the mono-energetic beam and for $\delta = 9$ and $E_c < 4 \text{ keV}$ the results were more well-defined, and therefore no spread is indicated in Figure 5.

Taking the thermal energy calculated previously for the jet, over the time range considered here the required heating power is $6.18 \times 10^{22} \text{ erg s}^{-1}$. This

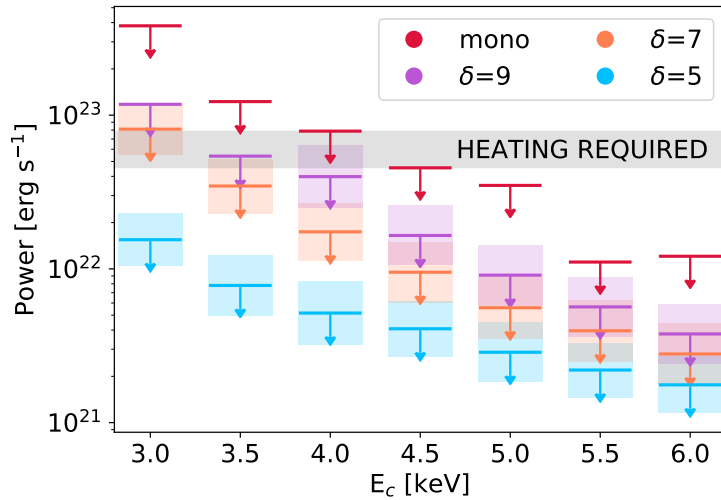


Figure 5. Upper limits on the non-thermal heating power for a range of E_c and δ ($= 5, 7, 9$, and a mono-energetic beam) values. The shaded regions indicate the $\pm 1 \sigma$ range of the Gaussian distribution fitted to the upper limit results. The grey shaded area indicates the heating requirement dictated by the NuSTAR thermal emission, with the range determined from the uncertainties on the fit temperature and emission measure.

heating requirement is marked on the plot with the non-thermal upper limits in Figure 5. This demonstrates that the non-thermal emission would have to be very steep, almost mono-energetic, between 3 and 4 keV to power the required heating as determined from the NuSTAR thermal emission.

2.2. Bright Limb Emission

The brightest, and also largest, source that appears in the NuSTAR mosaics in Figure 1 is the emission from the east limb. As seen in the SDO/AIA and Hinode/XRT images, this NuSTAR feature is in fact comprised of emission from two different sources: a bright loop, and surrounding diffuse emission. Looking back to two solar rotations before this observation, this area was the site of a SPoCA active region (Delouille *et al.*, 2012) (though it is too faint to be a NOAA active region), so this bright emission is likely due to the presence of a decayed active region. From SDO/AIA images from days following this observation, as the Sun rotates this bright region is followed by a coronal hole.

This source is captured fully by P11 and partially by P10 and 20 in both NuSTAR orbits. Figure 6 shows the NuSTAR images of this region from P11 of orbits 1 and 2, with FPMA and FPMB shown separately. This limb emission is relatively bright and extended, meaning that the SNR is not as big of an issue as it is with the other features. However, there are other factors which complicate the fitting of its NuSTAR spectra. Firstly, in each of the pointings this source is extended enough to be positioned over multiple NuSTAR detector quadrants, which have varying responses. Also, as mentioned previously, the NuSTAR emission is a combination of the bright loop and the surrounding diffuse

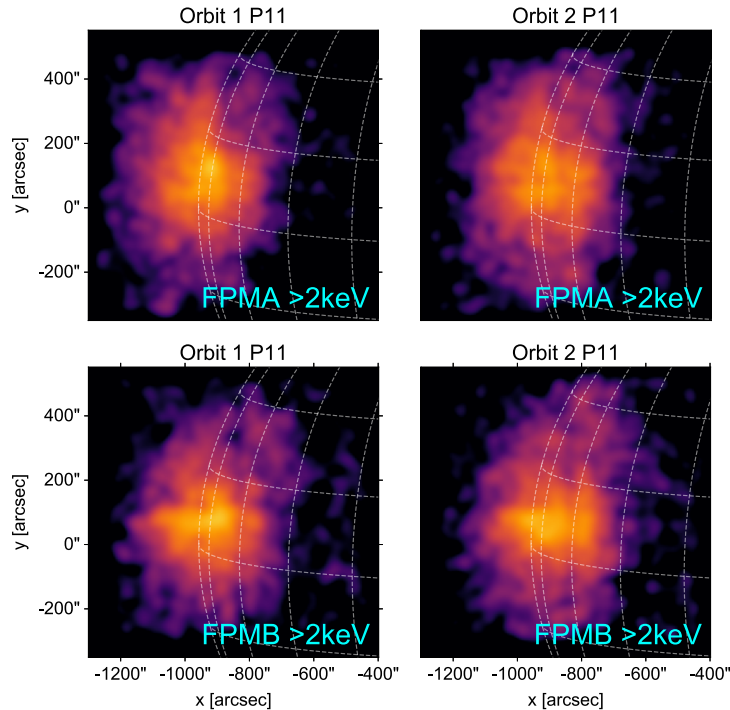


Figure 6. NuSTAR FPMA (top) and FPMB (bottom) images of the bright limb emission from P11 of orbit 1 (18:48:35–18:50:16 UT) and orbit 2 (20:25:15–20:26:56 UT).

emission. Therefore, in order to investigate the properties of the emission that originates only from the bright loop in SDO/AIA and Hinode/XRT, the brightest section of the NuSTAR emission was chosen for the fitting.

However, this bright loop is not ideally positioned in most of the pointings that capture this area. P20 of both orbits captures the bottom half of this region, with the edge of the FOV just missing the bright loop. In orbit 2, the bright loop lies just off the edge of the detector in P10 and across a detector gap in P11 in both FPMA and FPMB, resulting in these counts being lost. This effect is demonstrated in Figure 6, where the detector gaps are visible. These problems are also encountered in both pointings in orbit 1 for FPMB. However, the bright loop lies within the FOV in P10 and P11 in FPMA, and therefore this feature can be seen in the top left panel of Figure 6. Consequently, the spectral analysis of this feature only includes these two pointings for FPMA only.

A circular region of radius $41''$, chosen such that only the brightest NuSTAR emission was enclosed, was used for the spectral fitting. Figure 7 shows the NuSTAR FPMA fitted spectrum for this source, with spectra from P10 and 11 from orbit 1 fit simultaneously. This spectrum was again fit with an isothermal model, giving a temperature of 2.53 MK and an emission measure of $9.62 \times 10^{44} \text{ cm}^{-3}$. Because it is only possible to do a NuSTAR spectral fit for one point in time for this feature, and because this temperature once again lies above the peak

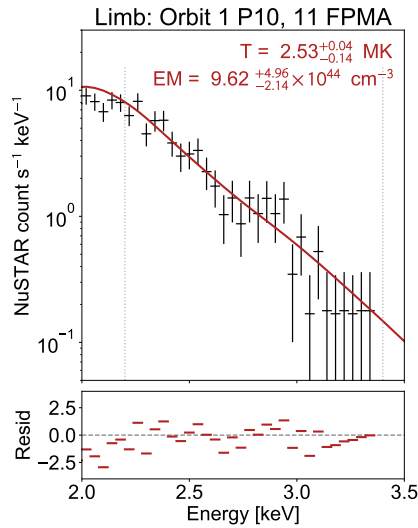


Figure 7. NuSTAR spectral fit for the bright loop on the east limb for NuSTAR orbit 1, FPMA only. This fit combines P10 (18:46:07–18:47:48 UT) and 11 (18:48:35–18:50:16 UT) from this orbit.

of SDO/AIA 211Å’s sensitivity, comparison with SDO/AIA and Hinode/XRT is difficult here.

2.3. Loops and Bright Point Near Disk Centre

In both orbits, NuSTAR observes a source near the centre of the the solar disk. Upon inspection of the SDO/AIA 211 Å and Hinode/XRT Be-thin images, shown in Figure 8, it can be seen that the NuSTAR emission in fact originates from two distinct sources: a perpendicular pair of loops, and a bright point which lies nearby, labelled BP3 in Figure 1.

Each of these features were captured in P13, 14, 17, and 18 in both of the NuSTAR orbits. For both the loops and BP3, The NuSTAR FPMA and FPMB spectra for these four pointings were fit simultaneously for each orbit. From the resulting fits, shown in Figure 9, the temperature of the loops decreases from 2.51 MK in the first orbit to 2.07 MK in the second, with the emission measure increasing from $1.03 \times 10^{44} \text{ cm}^{-3}$ to $6.39 \times 10^{44} \text{ cm}^{-3}$. However, when the uncertainties on these values are taken into account, any change in temperature and emission measure between the orbits is marginal for this feature. For the bright point, the fits also suggest a decrease in temperature, from 3.22 MK to 2.56 MK, with the emission measure increasing from $1.33 \times 10^{43} \text{ cm}^{-3}$ to $5.10 \times 10^{43} \text{ cm}^{-3}$.

3. Emerging Flux Region

The EFR, which later went on to become an active region, was observed by NuSTAR in both orbits. For this EFR, flux first begins to emerge just after 00:00

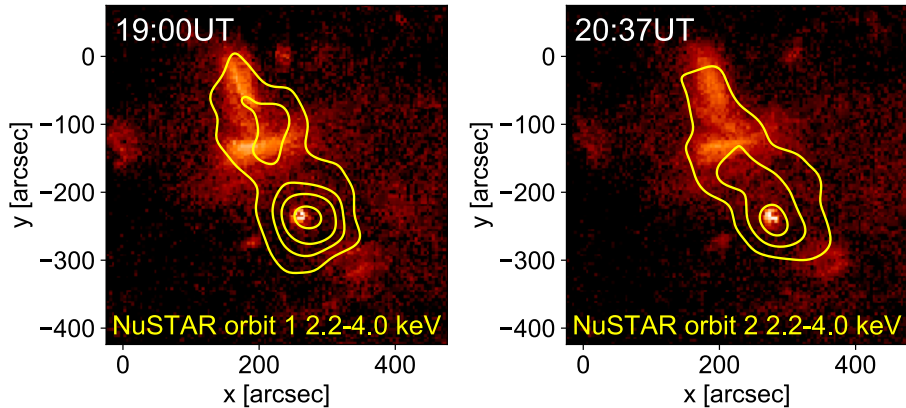


Figure 8. Hinode/XRT images of the loops and bright point near disk centre from orbits 1 and 2 (left and right, respectively). The aligned 2.2–4.0 keV NuSTAR contours are summed over P13, 14, 17, and 18 for each orbit, and are plotted at the same levels in both images ($4, 7, 10, 15 \times 10^{-4}$ counts s^{-1}).

UT on 28 September. There is some cancellation between opposite polarities, and the positive and negative polarities then spread apart. This is the time during which this feature is observed by NuSTAR. The next day, beginning at $\sim 14:00$ UT on 29 September, there is more intense flux emergence in this region, producing an active region.

In each NuSTAR orbit, the EFR was captured in four pointings, split into two pairs of consecutive pointings: 12 and 13, and 18 and 19. Capturing this feature four times in each orbit, for a total number of eight pointings over the whole observation, gives the opportunity to study its temporal evolution despite the short duration of the mosaic pointings.

Hinode/XRT Be-thin and SDO/AIA 211 \AA images of the EFR are shown in Figure 10. These images are from the mid-times of all of the mosaic pointings where NuSTAR captured the EFR. The NuSTAR 2.2–4.0 keV contours, aligned with SDO/AIA, are also plotted in this figure to show the HXR evolution of the feature. These contours indicate that the feature is generally brighter in the second orbit than the first. In the Hinode/XRT and SDO/AIA images, the EFR appears to be comprised of three separate regions. It is clear that the majority of the NuSTAR emission originates from the bright central region ($-250'', -250''$), particularly in the second orbit when the feature has brightened. However, there does appear to be a contribution from the upper region ($-300'', -200''$) to the NuSTAR emission in P12 of the first orbit, as shown in the top left panel for each instrument of Figure 10. The lower region ($-350'', -350''$) does not appear to contribute significantly to the NuSTAR emission. This is expected in P12 and 13 of each orbit, as this region would be outside NuSTAR’s FOV. In P18 and 19, this feature would lie close to a detector gap, which could explain the lack of NuSTAR emission from this region.

The Hinode/XRT Be-thin and SDO/AIA 211 \AA lightcurves for the EFR are plotted in Figure 11, including lightcurves for each region separately, and also

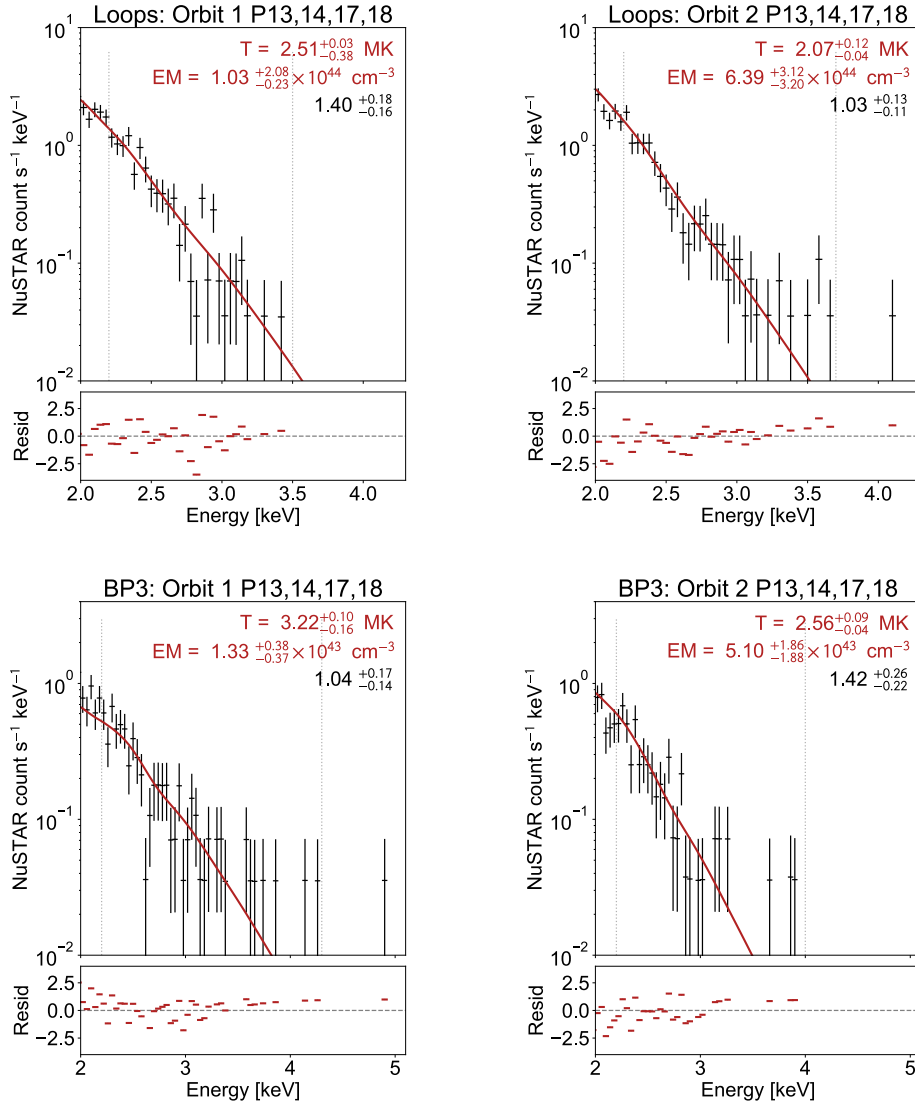


Figure 9. NuSTAR fitted spectra for the loops near disk centre (top) and the nearby bright point (bottom) simultaneously fitting FPMA and FPMB from P13, 14, 17, and 18 for both orbits (pointings lie between 18:53:29–19:07:24 UT in orbit 1; 20:30:09 – 20:44:04 UT in orbit 2). The number in black is the multiplicative constant introduced to account for systematic differences between FPMA and FPMB.

for the EFR as a whole with all three of the regions combined. These lightcurves were calculated over the rectangular boxes shown in the top left panel in Figure 10, chosen such that the sources remained in the boxes throughout the NuSTAR observation period. These lightcurves confirm that the central region is the brightest of the three in both SDO/AIA and Hinode/XRT, and the greatest contributor to the emission from the EFR as a whole, as shown in the top row

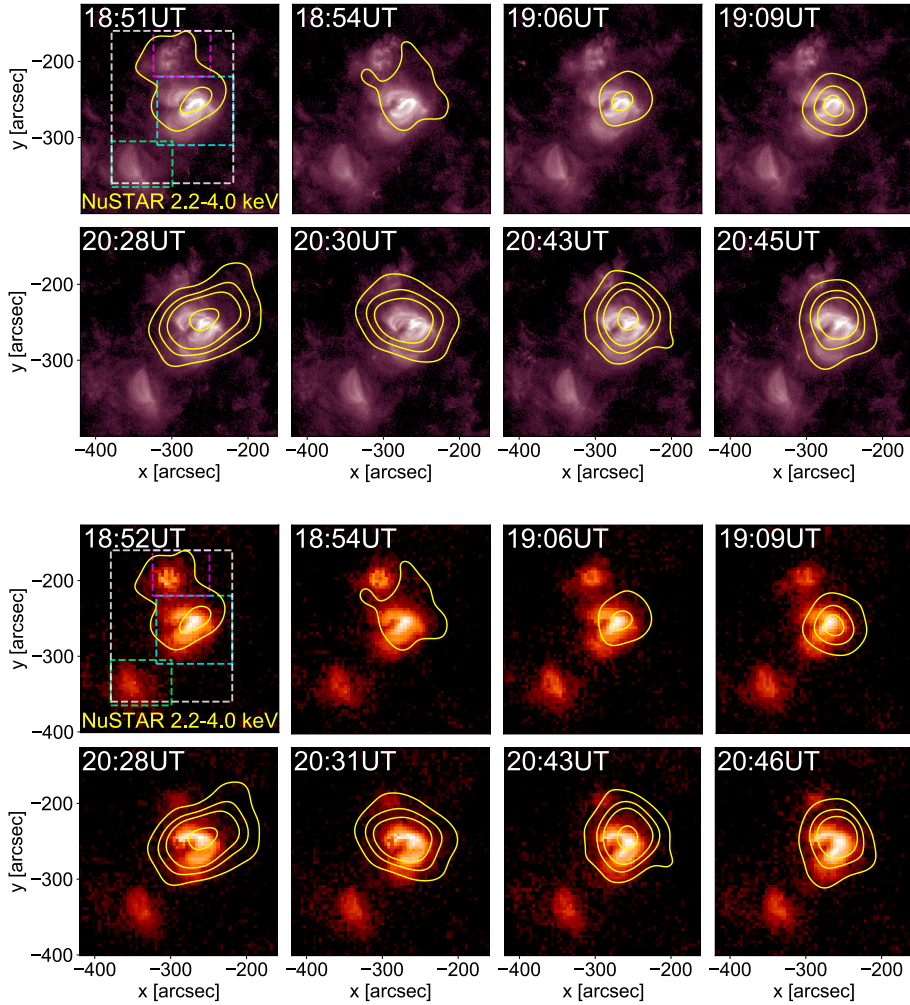


Figure 10. SDO/AIA 211Å (top two rows) Hinode/XRT Be-thin (bottom two rows) images of the EFR from the mid-times of the eight NuSTAR pointings that capture the feature. Yellow contours represent aligned NuSTAR FPMA + FPMB 2.2–4.0 keV, with the contours plotted at the same levels in all panels ($5, 10, 15, 30 \times 10^{-4}$ counts s^{-1}). For each instrument, the top row shows orbit 1 and the bottom shows orbit 2, with P12, 13, 18, 19 arranged from left to right. The dashed lines indicate the regions that the lightcurves in Figure 11 are calculated over.

of Figure 11. In the first orbit, both lightcurves for this region decrease between the times of the NuSTAR pointings (18:53 UT and 19:07 UT). Interestingly, between the two NuSTAR pointing times in the second orbit (20:29 UT and 20:44 UT) the Hinode/XRT lightcurve decreases where the SDO/AIA 211 Å lightcurve increases. However, the change in the SDO/AIA 211 Å lightcurve is relatively much smaller than the change in Hinode/XRT.

The Hinode/XRT lightcurve for the upper region shows a sharp peak in brightness during P12 of the first NuSTAR orbit, before falling off. This is

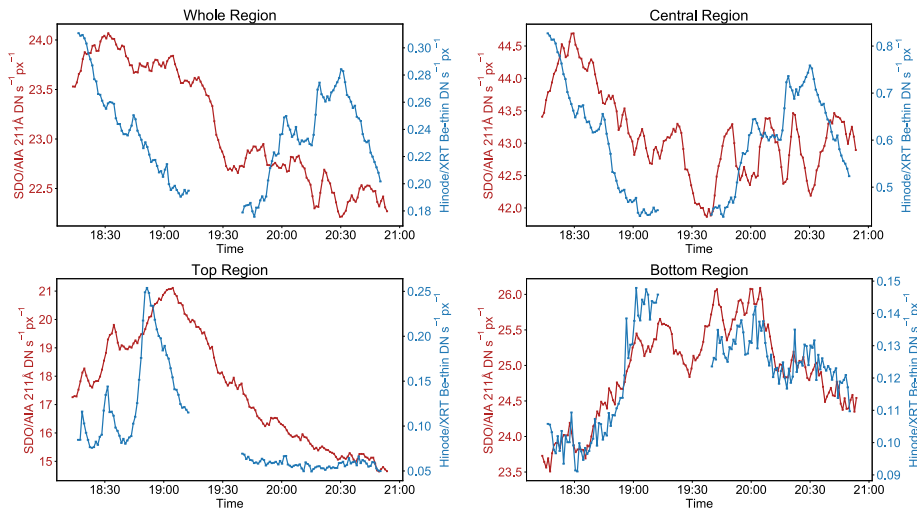


Figure 11. Hinode/XRT Be-thin (blue) and SDO/AIA 211 Å (red) lightcurves for the whole EFR, as well as the three separate regions within it. The green shaded areas indicate the times of the eight NuSTAR mosaic pointings that captured the EFR.

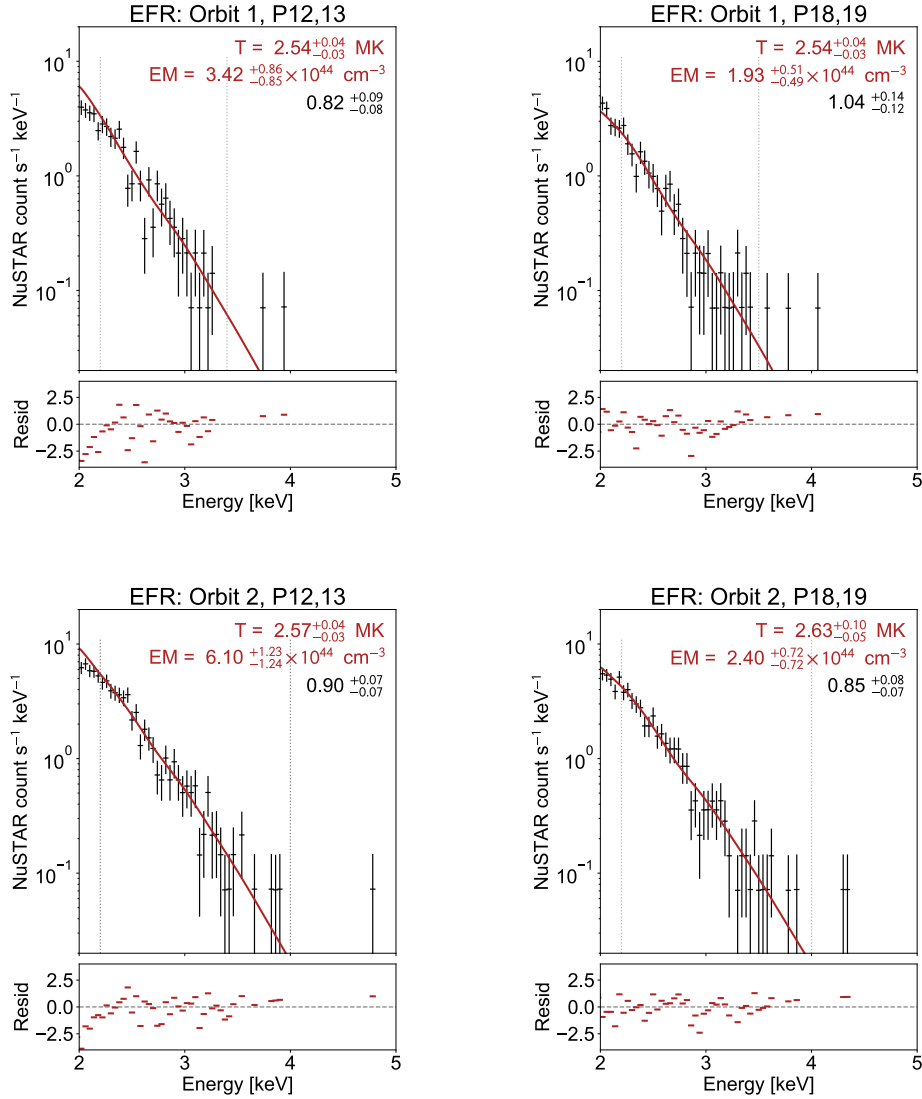
consistent with the NuSTAR contours in the top left panel for each instrument in Figure 10, where the upper region is significantly contributing to the NuSTAR emission in P12 of orbit 1. The peak in the Hinode/XRT lightcurve followed later by the peak in the SDO/AIA 211 Å lightcurve for this region suggests a heating of material followed by cooling.

The lower region is outside NuSTAR’s FOV in P12 and 13, and would be positioned near or on a detector gap in P18 and 19. However, the lightcurves confirm that this feature is relatively very faint in Hinode/XRT in comparison to the central region, and therefore would be unlikely to contribute significantly to the NuSTAR emission from the EFR.

3.1. NuSTAR Spectral Analysis

The EFR was observed in P12, 13, 18, and 19 in each orbit. Including FPMA and FPMB, this gives a total of 16 spectra that could be fit simultaneously or separately. When fitting the spectra of the faint NuSTAR mosaic features, it is important to find a balance between combining enough spectra to get a good fit and being able to obtain information about how the feature evolves over time. This is particularly true in the case of the EFR, a source for which the temporal evolution is of interest. To ensure that the properties of the EFR did not change significantly between the pointings being used, the spectra for the two pairs of consecutive pointings, 12 and 13, and 18 and 19, were fit simultaneously for each orbit. For this feature, the circular region used for the fitting had a radius of 83.5″.

The NuSTAR spectra for the EFR and their fits are shown in Figure 12. Each of these spectra are well fit with a single isothermal APEC model, and show no evidence of non-thermal emission or a higher temperature component.



The spectral fits from all four times give a reasonably constant temperature of ~ 2.5 MK, and emission measures ranging between 1.9 and $6.1 \times 10^{44} \text{ cm}^{-3}$. The fits do suggest a slight increase in temperature of the EFR over the two orbits, from 2.54 MK to 2.63 MK. However, taking into account the uncertainties on these temperatures, this increase is not statistically significant. The emission measure from the spectral fits decreases from 3.42 to $1.93 \times 10^{44} \text{ cm}^{-3}$ between P12,13 and P18,19 in the first orbit (as seen in the top row of Figure 12). It then

increases up to $6.10 \times 10^{44} \text{ cm}^{-3}$ in P12,13 in the second orbit, before falling to $2.40 \times 10^{44} \text{ cm}^{-3}$ for P18,19 (as seen in the bottom row of Figure 12). This behaviour is broadly similar to that observed in the Hinode/XRT lightcurve for the central region in Figure 11. In both orbits, the NuSTAR fit temperature remains approximately constant while the emission measure decreases. This is in agreement with the decreases in the Hinode/XRT lightcurve between the NuSTAR pointing times in both orbits, and the highest NuSTAR emission measure corresponds to the highest peak in Hinode/XRT at 20:30 UT. This similar behaviour is expected as Hinode/XRT and NuSTAR should be observing emission at approximately the same temperatures.

3.2. Differential Emission Measures

In the EFR lightcurves in Figure 11, at around 20:30 UT (NuSTAR orbit 2, P12 and 13), there is a peak in the Hinode/XRT Be-thin lightcurve that coincides with a minimum in the SDO/AIA 211 Å lightcurve. Later, at around 20:45 UT (NuSTAR orbit 2, P18 and 19) there is increased SDO/AIA 211Å emission but decreased Hinode/XRT Be-thin emission. As Hinode/XRT is sensitive to higher temperature emission than SDO/AIA 211 Å, this suggests that there is more higher temperature emission present at 20:30 UT than at 20:45 UT. In order to confirm this we perform differential emission measure (DEM) analysis.

In an effort to understand the multi-thermal nature of this feature, we reconstruct DEMs for the EFR for each orbit, combining data from NuSTAR, Hinode/XRT, and the six SDO/AIA optically thin coronal-temperature channels. As with the spectral fitting, we consider NuSTAR P12 and 13, and P18 and 19 for each orbit jointly by averaging both the NuSTAR data values and responses for the two pointings. Recovering the DEM involves solving the ill-posed inverse problem $g_i = K_{i,j} DEM(T)$, where g_i [$\text{DN s}^{-1} \text{ px}^{-1}$] is the observed flux in each channel, and $K_{i,j}$ is the temperature response for the i^{th} channel and the j^{th} temperature bin. The regularized inversion approach of Hannah and Kontar (2012) was used to reconstruct the DEMs for the EFR, using the minimum of the EM loci curves for weighting.

The fluxes for SDO/AIA and Hinode/XRT were obtained from an image from each channel averaged over the relevant NuSTAR pointing time, using only the central region of the EFR (as in Figure 10). A systematic error of 20% was assigned to the SDO/AIA, Hinode/XRT, and NuSTAR fluxes in order to account for uncertainties in their temperature responses. The photon shot noise was calculated for all three instruments. In the case of SDO/AIA and Hinode/XRT, this uncertainty was found to be negligible compared to the systematic uncertainty as this flux was calculated as an average over all of the pixels that capture the EFR. However, in the case of NuSTAR, the shot noise was not negligible, and therefore was added in quadrature with the 20% systematic error. For the DEM calculation, the NuSTAR data was split into two energy bands: 2.2–2.6 keV and 2.6–3.6 keV. The SDO/AIA and Hinode/XRT temperature responses were calculated using the standard Solarsoft routines from the instrument teams: `aia_get_response.pro` for SDO/AIA and `make_xrt_temp_resp.pro` for Hin-

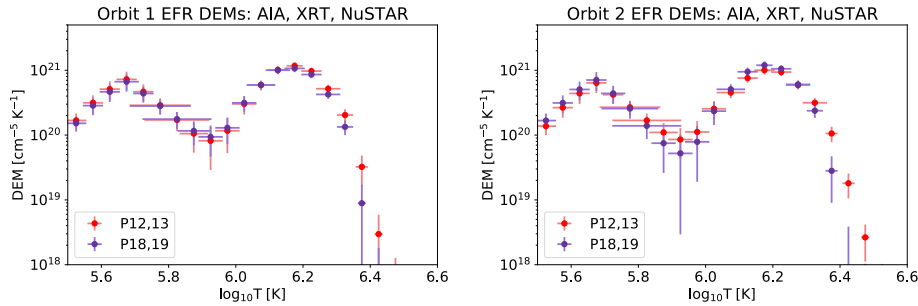


Figure 13. DEMs for the EFR for NuSTAR orbit 1 (left) and orbit 2 (right), combining P12 and 13 (red) and P18 and 19 (purple). These DEMs are reconstructed using data from NuSTAR, Hinode/XRT and SDO/AIA.

ode/XRT. The NuSTAR response was calculated in Python² using the spectral responses used in section 3.1.

DEM analysis combining data from NuSTAR, SDO/AIA and Hinode/XRT has been done before by Wright *et al.* (2017). In this study, it was found that multiplying the Hinode/XRT responses by a factor of 2 before calculating the DEMs produced a solution with smaller residuals. This choice was made following the suggestion of previous authors who also found discrepancies when using Hinode/XRT data (Schmelz *et al.*, 2015; Testa *et al.*, 2011; Cheung *et al.*, 2015). In the case of the EFR, the DEMs were calculated using the Hinode/XRT responses both with and without an added multiplicative factor of 2. Introducing this factor was similarly found to improve the DEM results here, and so was used for all of the DEMs shown.

A comparison between the DEMs calculated for P12 and 13, and P18 and 19 is shown for each orbit in Figure 13. In orbit 1, between these two times, the emission in both the Hinode/XRT Be-thin and SDO/AIA 211 Å lightcurves in Figure 11 decreases, though the change in brightness is smaller than the 20% systematic error used in the DEM calculation in both cases. This is reflected in the two DEMs for these times, as the DEM for P12 and 13 is higher than the one for P18 and 19 for $\log(T)$ higher than ~ 6.2 , though they are not significantly different when taking into account the error bars.

In the case of orbit 2, the Hinode/XRT lightcurve shows a peak at around the time of NuSTAR P12 and 13, before decreasing for NuSTAR P18 and 19. Between these two times, the decrease in Hinode/XRT emission and corresponding increase in SDO/AIA 211 Å emission suggests that there is hotter material present at the earlier time. The change in Hinode/XRT is higher than the 20% systematic errors, whereas the change in 211 Å is again very small. From the calculated DEMs, there is more emission above $\log(T) \sim 6.3$ at the earlier time, in agreement with the fall-off in the Hinode/XRT lightcurve. The DEM for P18 and 19 is higher than that for P12 and 13 for $\log(T)$ between ~ 6.1 and 6.3, though there is no difference between the DEMs at these temperatures outwith

²https://github.com/ianan/nustar_sac/blob/master/python/ns_tresp.py

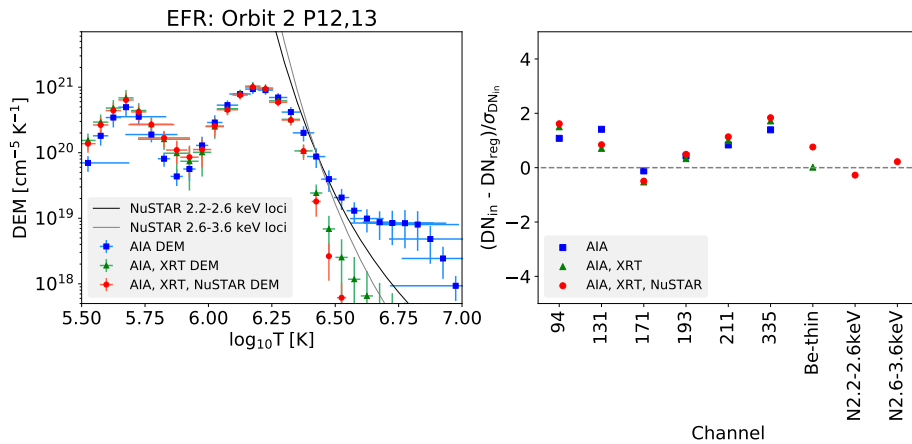


Figure 14. An example of a DEM reconstructed using data from SDO/AIA only (blue), from SDO/AIA and Hinode/XRT (green), and from SDO/AIA, Hinode/XRT and NuSTAR (red). The NuSTAR EM loci curves are also plotted in grey.

the error bars. Material at these temperatures could be responsible for the peak in the SDO/AIA 211Å at the later time.

Adding X-ray data to a DEM calculation using SDO/AIA is useful in constraining the higher temperature emission. Figure 14 shows a comparison between one of the EFR DEMs (from orbit 2 P12 and 13) reconstructed using data from SDO/AIA only, from SDO/AIA and Hinode/XRT, and from SDO/AIA, Hinode/XRT, and NuSTAR. In addition to the three DEMs plotted here, a DEM was also reconstructed using data from SDO/AIA and NuSTAR only. It was found that the solution was consistent within the error bars with the DEM including all three instruments. In this figure, the NuSTAR EM loci curves are marked on. The point of intersection between the loci curves for the two energy bands corresponds to the T and EM values from the NuSTAR spectral fit.

All three of the DEMs in Figure 14 peak at $\log(T) \sim 6.15$, and are in good agreement below $\log(T) \sim 6.4$. This figure demonstrates that the addition of Hinode/XRT to the calculation helps to constrain the DEM at temperatures higher than this, and adding NuSTAR strengthens this constraint. From including the X-ray data rather than relying on SDO/AIA alone, it is clear that there is virtually no emission above 4 MK here. Previous studies looking at non-flaring active regions and using different DEM approaches to those used in this paper also found that erroneous higher temperature DEM components could appear if HXR data was not included (Schmelz *et al.*, 2009; Reale, McTiernan, and Testa, 2009).

A previous study of an EFR in the quiet Sun by Kontogiannis *et al.* (2020) also included DEM analysis, using data from Hinode/EIS. The results from this study agree with the results found here, with both finding a DEM peak of comparable magnitude at a similar temperature ($\log(T) \sim 6.1$). Using only data from Hinode/EIS, this study obtained solutions that were not well-defined for $\log(T) > 6.3$. Including the X-ray data here provides a constraint at higher temperatures to produce a more well-defined solution in this range.

3.3. NuSTAR Non-thermal Upper Limits

Using the approach detailed in section 2.1.1, the upper limits on any non-thermal emission present in the EFR were calculated and compared to the required heating power obtained from the thermal energy of the plasma. This calculation was done for the peak time in the Hinode/XRT lightcurve, corresponding to NuSTAR orbit 2 P12 and 13. The central region of the EFR is $\sim 35''$ square and therefore, following the same approach as for the jet, has a volume of $1.65 \times 10^{28} \text{ cm}^3$. Using equation 1 and the fit values from the spectrum in Figure 12, its thermal energy is $3.37 \times 10^{27} \text{ erg}$, with a heating power of $1.37 \times 10^{25} \text{ erg s}^{-1}$ over the observation time.

It was found that none of the upper limits on the non-thermal power were consistent with the required heating power. The area used here may have been an over-estimate, and making this value smaller would in turn lower the heating requirement. However, even reducing the area by 50% results in a required heating power that is reduced by less than a factor of 2, and this power is an order of magnitude larger than the upper limits on the non-thermal heating power. Therefore, it can be concluded that, in the case of the EFR, any non-thermal component that is present is not responsible for the observed heating.

4. Bright Points

Two bright points, labelled BP1 and BP2 in Figure 1, were observed with NuSTAR, and also with Hinode/XRT and SDO/AIA. Figure 15 shows Hinode/XRT and SDO/AIA 211 Å images, with aligned NuSTAR contours, of the bright points from the time of P17 of the second NuSTAR orbit. In both 211 Å and Hinode/XRT, BP2 is a more compact feature than BP1, but it is brighter in NuSTAR at this time.

BP1 is observed with NuSTAR in P14, 15, 16, and 17 of both orbits. BP2 is close to BP1, and lies in a region that is captured by NuSTAR also in P14, 15, 16, and 17. However, this feature is extremely faint in the first orbit, making it unusable for spectroscopy. Though it is present in all pointings in orbit 2, BP2 is located over the edge of the detector in P14 and 15, and is therefore only well observed in P16 and 17.

The SDO/AIA 211Å and Hinode/XRT Be-thin lightcurves for the two bright points are shown in Figure 16. These lightcurves were calculated over the boxes enclosing the bright points shown in Figure 15. In the case of BP1, the lightcurves indicate an increase in brightness in both channels, peaking just before the NuSTAR pointings in the first orbit, and then they continue to increase in brightness until the pointings in the second orbit. The two lightcurves for BP2 also show increasing brightness throughout both orbits of NuSTAR observation. This behaviour explains why BP2 is not observed by NuSTAR in the first orbit; it is not yet producing sufficiently bright emission to be detected by NuSTAR.

4.1. NuSTAR Spectral Analysis

In order to investigate the properties of both of these features, the NuSTAR spectra of the bright points were fitted. As was the case with the EFR, the

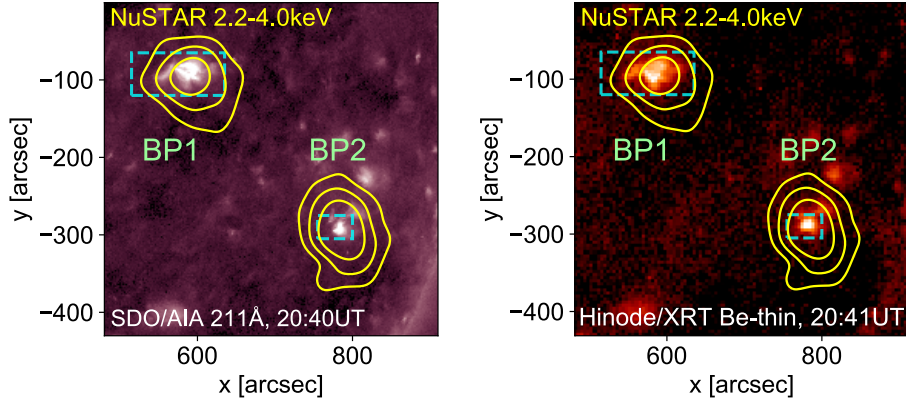


Figure 15. SDO/AIA 211 Å (left) and Hinode/XRT Be-thin (right) images of the two bright points from 20:41 UT, coinciding with NuSTAR orbit 2 P17. Yellow contours represent NuSTAR 2.2–4.0 keV (contour levels are 5, 10, 20 $\times 10^{-4}$ counts s^{-1}), aligned with SDO/AIA. The dashed boxes indicate regions used for obtaining the lightcurves in Figure 16.

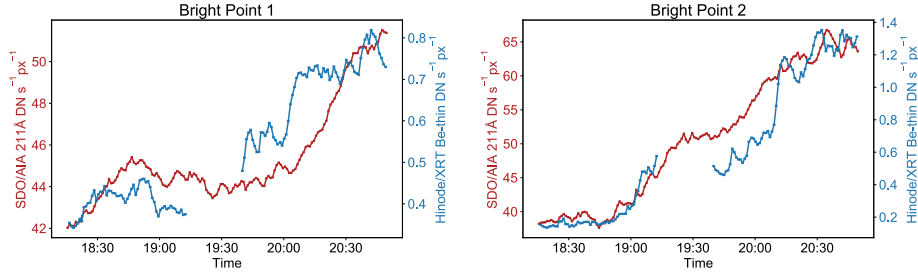


Figure 16. SDO/AIA 211 Å (red) and Hinode/XRT (blue) Be-thin lightcurves for BP1 (left) and BP2 (right). The green shaded areas indicate the times of the NuSTAR pointings suitable for spectroscopy.

spectra from individual pointings for these features are noisy and poorly fit due to their faintness and the short integration time. Therefore, spectra from multiple pointings were fit simultaneously (also combining FPMA and FPMB) to improve the SNR. In the case of both bright points, the spectra were fit using an isothermal APEC model, once again fitting down to 2.2 keV. The circular regions used for the fitting had radii of $68''$ and $47''$ for BP1 and BP2 respectively.

For BP1, a NuSTAR spectrum was fit for each orbit, combining data from P14, 15, 16, and 17 for both. The resulting fits, shown in Figure 17, indicate that this feature has a temperature of ~ 2.5 MK, with the emission measure increasing from 1.14 to 4.07×10^{44} cm^{-3} between the two orbits. This increase in emission measure is in agreement with the increase in brightness shown in the Hinode/XRT and SDO/AIA lightcurves in Figure 16. Considering both the fits and the lightcurves, NuSTAR sees an increase in EM by a factor of ~ 4 , while the feature brightens by a factor of ~ 1.2 in SDO/AIA 211 Å and ~ 2 in Hinode/XRT Be-thin. This could be due to both of these channels, 211 Å in particular, being also sensitive to cooler material than NuSTAR, meaning that

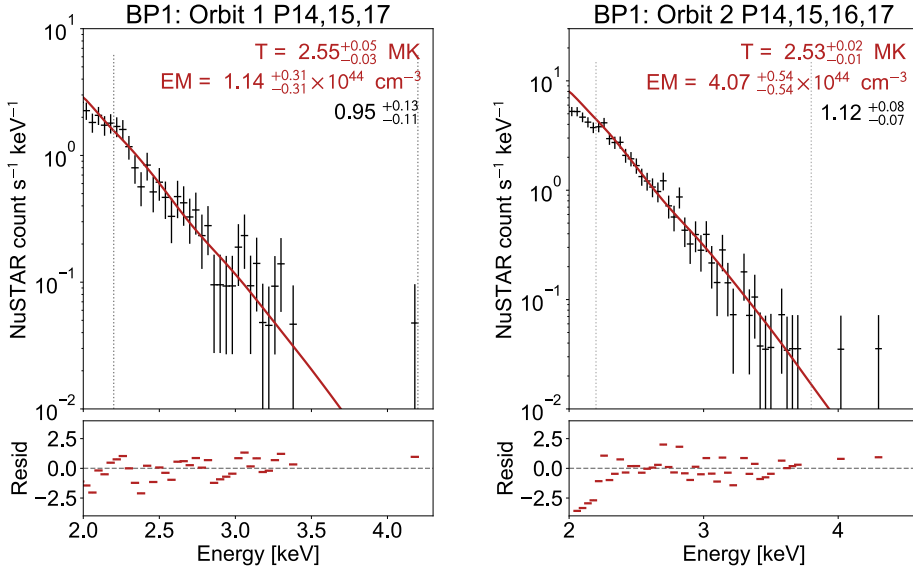


Figure 17. NuSTAR spectral fits for BP1 for NuSTAR orbits 1 and 2. NuSTAR FPMA and FPMB spectra from P14, 15, 16, and 17 are fit simultaneously for both orbits (pointings lie between 18:55:56–19:04:56 UT in orbit 1; 20:32:36 – 20:41:36 UT in orbit 2). The number in black is the multiplicative constant introduced to account for systematic differences between FPMA and FPMB.

if this brightening is occurring at higher temperatures, it is less significant to the overall emission in these channels.

For BP2, which was only well observed in P16 and 17 in the second NuSTAR orbit, a spectrum containing these two pointings was fit, with the resulting plot shown in Figure 18. The fit values for the temperature and emission measure of this spectrum are 3.22 MK and $5.98 \times 10^{43} \text{ cm}^{-3}$, respectively. These fit parameters indicate that the NuSTAR emission from BP2 originates from a hotter temperature than for BP1. The spectra for both bright points are well fit with the isothermal model and, similarly to the previous examples, do not show any evidence of either a higher temperature or non-thermal component.

4.2. Differential Emission Measures

Following the approach of section 3.2, differential emission measures were reconstructed for both BP1 and BP2 in order to further investigate the temperature difference between the two bright points that is apparent in their NuSTAR spectral fits. BP1 was observed in both NuSTAR orbits, and a combined DEM was obtained for this feature for each. As was the case with the spectra shown in Figure 17, these DEMs were reconstructed by combining data from P14, 15, 16, and 17 of each orbit. The DEM for BP2 was calculated using combined data from P16 and 17 from the second orbit only. Several of the Hinode/XRT Be-thin pixels which covered BP2 were saturated at the times of these pointings, so only SDO/AIA and NuSTAR data were included in the DEM calculation for

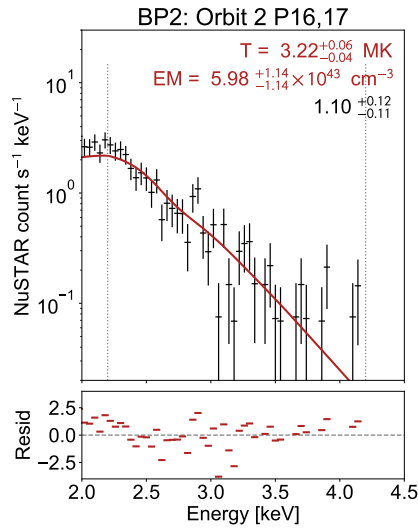


Figure 18. NuSTAR spectral fit for BP2 for NuSTAR orbit 2. This fit combines P16 (20:37:31–20:39:12 UT) and 17 (20:39:58–20:41:36 UT), FPMA and FPMB, from this orbit. The number in black is the multiplicative constant introduced to account for systematic differences between FPMA and FPMB.

this feature (though including Hinode/XRT was found to not change the shown solution significantly).

All three of the resulting DEMs are plotted in Figure 19. The brightening in BP1 between the two orbits seen in Figure 16 is reflected in the DEMs for this feature. The DEM for orbit 2 is higher than for orbit 1 for $\log(T) \geq 6.2$, which is consistent with the observed brightening.

Compared to the 2.5 MK NuSTAR fit temperature for BP1, a temperature of 3.2 MK was found when fitting the NuSTAR spectrum for BP2. The DEM for BP2 is higher than the ones for BP1 for $\log(T) > 6.2$, and it extends to higher temperatures. This suggests that there is more high temperature emission present in this bright point, which explains the higher fit temperature found for BP2 in the NuSTAR spectroscopy.

The DEMs for both of the bright points have a peak at $\log(T) \sim 6.15$, a result which has also been found in previous DEM analyses of coronal bright points (Brosius *et al.*, 2008; Doschek *et al.*, 2010). Similarly to the case of the EFR, the DEMs of both bright points confirm that there are no higher temperature components, with no significant emission present above 4 MK. Once again, these DEMs benefit from using the X-ray data from NuSTAR and Hinode/XRT to constrain the higher temperature emission.

4.3. NuSTAR Non-thermal Upper Limits

Again following the approach from section 2.1.1, the non-thermal upper limits were calculated for BP1 and BP2, both for orbit 2 when they were at their brightest in NuSTAR. For BP1, which is $35''$ square and therefore has an associated volume of $1.65 \times 10^{28} \text{ cm}^3$, the thermal energy was found to be $2.71 \times$

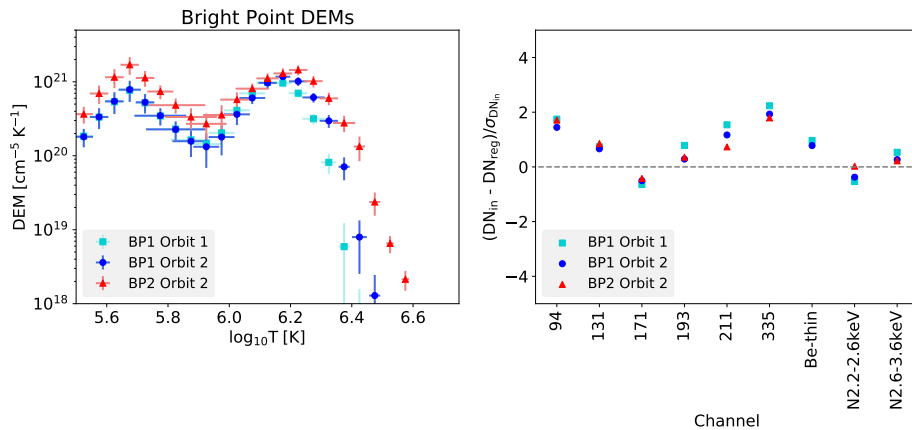


Figure 19. DEMs for the two bright points. The DEMs for BP1 in orbits 1 (light blue) and 2 (dark blue) were reconstructed using data from SDO/AIA, Hinode/XRT, and NuSTAR. The DEM for BP2 in orbit 2 (red) was reconstructed using data from only SDO/AIA and NuSTAR (due to saturation in Hinode/XRT Be-thin).

10^{27} erg, giving a heating power of 5.02×10^{24} erg s^{-1} . The largest non-thermal upper limits for BP1 were about an order of magnitude smaller than the heating requirement. If there was some filling factor < 1 and the area used here was an overestimate, then the heating requirement could be reduced. However, BP1 would still be at the very limit of being a possible non-thermally heated source.

BP2, which was $15''$ square with a volume of 1.30×10^{27} cm^3 , has a thermal energy of 3.71×10^{26} erg, meaning the heating power is 1.52×10^{24} erg s^{-1} . The upper limits on the non-thermal heating power are only slightly lower than this value for a very steep, almost mono-energetic, spectrum with a low energy cutoff of ~ 3 keV. Again, the heating requirement could be shifted down by using a filling factor < 1 and reducing the area. Therefore, it is possible that this feature could have been heated non-thermally, but this result is marginal.

5. Discussion and Conclusions

In this paper, we have presented the first survey of quiet Sun features in HXRs observed during solar minimum. NuSTAR’s full-disk solar mosaic mode allowed for a range of different types of features to be observed. In these two mosaics, NuSTAR observed steady features, such as bright points and an EFR, but also captured a transient jet. This is the first observation of these types of features using a HXR focusing telescope. The mosaics also reveal large-scale sources (the diffuse sources in Figure 1), diagnostically important for investigating the heating of the diffuse corona.

From fitting the NuSTAR spectra of these features, we find their temperatures lie in the range 2.0–3.2 MK, but we find no evidence of a higher temperature or non-thermal component present in their X-ray spectra. We have used EUV and SXR data from SDO/AIA and Hinode/XRT in addition to NuSTAR to investigate the temperature evolution of the quiet Sun features, including successfully

reconstructing DEMs which combine data from all three of these instruments. The DEM solutions for these quiet Sun features show no evidence of emission above 4 MK, a result achieved by using X-ray data in the DEM calculation to constrain the solution at high temperatures.

The temperatures found from the NuSTAR spectral fits for all of the features investigated here lie in a narrow temperature range between 2.0–3.2 MK. This is consistent with the findings from previous studies that used EUV and SXR data, which have found that bright point temperatures are generally < 3 MK (Doschek *et al.*, 2010; Alexander, Del Zanna, and Maclean, 2011; Kariyappa *et al.*, 2011). In the work presented in this paper we have also found two slightly hotter bright points (BP2 and BP3), with the NuSTAR spectral fit giving 3.2 MK. However, these studies have found that some bright points have temperatures < 2 MK when investigated using EUV and/or SXR data. Although NuSTAR is more sensitive to higher temperature emission, there is so little of it in these features that the spectra are dominated by these cooler sources, appearing effectively isothermal, capturing the 2–3 MK peak of the DEM.

Difficulties arise in this analysis when working with SDO/AIA data because none of the SDO/AIA channels have a peak in sensitivity in the 2–3MK range. As a result, the SDO/AIA 211 Å lightcurves for these features sometimes do not show behaviour consistent with Hinode/XRT or with NuSTAR. Previous analysis of microflares observed with NuSTAR (for example, Cooper *et al.* (2020, 2021)) has made use of the SDO/AIA Fe XVIII proxy channel (Del Zanna, 2013). Unfortunately, the temperatures of these quiet Sun features are too low for this to be useful. However, Hinode/XRT has sensitivity in a similar temperature range to NuSTAR, and makes a useful comparison.

As all of the NuSTAR spectra were adequately fitted with an isothermal model, only non-thermal upper limits were found for some of the features. In most cases, it was found that the possible non-thermal component was not sufficient to produce the required heating. The feature that was the best candidate for non-thermal heating was the jet. However, even this would require a very steep (effectively mono-energetic) non-thermal distribution with a low energy cutoff between 3–4 keV.

From the spectral, DEM, and non-thermal upper limit analysis performed here, it can be concluded that if there are any higher temperature or non-thermal sources in the features from this observation, they would have to be very weak. However, the NuSTAR full-disk solar mosaics, while useful in allowing the observation of multiple sources present within an orbit, have limitations when investigating the properties and evolution of these quiet Sun features. For these faint features, the short 100 s pointings combined with NuSTAR’s limited throughput (which is dominated by lower energy X-rays) makes it unlikely that higher temperature or non-thermal components that are present would be detectable unless they were relatively strong.

The work presented in this paper used the first NuSTAR quiet Sun campaign from the recent solar minimum. Additional data sets were taken throughout the solar minimum (2018–2020) in both the full-disk mosaic mode as well as longer dwells, in which pointing was not changed. In these dwells, any bright points would be observed for several hours over multiple orbits. These longer observing

campaigns could provide a better opportunity to detect more energetic HXR emission from the quiet Sun, and also increase the chances of capturing more atypical harder sources. Having observations of quiet Sun features over a longer period of time will also mean that a more rigorous investigation of their temporal evolution in HXR will be possible.

The NuSTAR quiet Sun dwell data will be used to further the work presented here, and will be the subject of future papers. However, shorter time-scale variability in the HXR emission from quiet Sun features such as these may remain difficult to detect until there is a dedicated solar X-ray instrument with higher sensitivity and throughput.

Acknowledgements This paper made use of data from the NuSTAR mission, a project led by the California Institute of Technology, managed by the Jet Propulsion Laboratory, funded by the National Aeronautics and Space Administration. We thank the NuSTAR Operations, Software and Calibration teams for support with the execution and analysis of these observations. This research made use of the NuSTAR Data Analysis Software (NUSTARDAS) jointly developed by the ASI Science Data Center (ASDC, Italy), and the California Institute of Technology (USA). Hinode is a Japanese mission developed and launched by ISAS/JAXA, with NAOJ as domestic partner and NASA and UKSA as international partners. It is operated by these agencies in co-operation with ESA and NSC (Norway). AIA on the Solar Dynamics Observatory is part of NASA's Living with a Star program. This research has made use of SunPy, an open-source and free community-developed solar data analysis package written in Python (SunPy Community *et al.*, 2015) This research made use of Astropy, a community-developed core Python package for Astronomy (Astropy Collaboration *et al.*, 2018, 2013)

Funding SP acknowledges support from the UK's Science and Technology Facilities Council (STFC) doctoral training grant (ST/T506102/1). IGH acknowledges support from a Royal Society University Fellowship (URF/R/180010) and STFC grant (ST/T000422/1).

Data Availability All the data used in this paper are publicly available. In particular, NuSTAR via the [NuSTAR Master Catalog](#) with the OBSIDs 90410101001 - 90410125001 and 90410201001 - 90410225001.

Declarations

Conflict of interest The authors declare that they have no conflicts of interest.

References

- Alexander, C.E., Del Zanna, G., Maclean, R.C.: 2011, Hinode observations and 3D magnetic structure of an X-ray bright point. *Astron. Astrophys.* **526**, A134. [DOI](#). [ADS](#).
- Alipour, N., Safari, H.: 2015, Statistical Properties of Solar Coronal Bright Points. *Astrophys. J.* **807**(2), 175. [DOI](#). [ADS](#).
- Arnaud, K.A.: 1996, XSPEC: The First Ten Years. In: Jacoby, G.H., Barnes, J. (eds.) *Astronomical Data Analysis Software and Systems V*, *Astronomical Society of the Pacific Conference Series* **101**, 17. [ADS](#).
- Astropy Collaboration, Robitaille, T.P., Tollerud, E.J., Greenfield, P., Droettboom, M., Bray, E., Aldcroft, T., Davis, M., Ginsburg, A., Price-Whelan, A.M., Kerzendorf, W.E., Conley, A., Crighton, N., Barbary, K., Muna, D., Ferguson, H., Grollier, F., Parikh, M.M., Nair, P.H., Unther, H.M., Deil, C., Woillez, J., Conseil, S., Kramer, R., Turner, J.E.H., Singer, L., Fox, R., Weaver, B.A., Zabalza, V., Edwards, Z.I., Azalee Bostroem, K., Burke, D.J.,

- Casey, A.R., Crawford, S.M., Dencheva, N., Ely, J., Jenness, T., Labrie, K., Lim, P.L., Pierfederici, F., Pontzen, A., Ptak, A., Refsdal, B., Servillat, M., Streicher, O.: 2013, Astropy: A community Python package for astronomy. *Astron. Astrophys.* **558**, A33. DOI. ADS.
- Astropy Collaboration, Price-Whelan, A.M., Sipőcz, B.M., Günther, H.M., Lim, P.L., Crawford, S.M., Conseil, S., Shupe, D.L., Craig, M.W., Dencheva, N., Ginsburg, A., VanderPlas, J.T., Bradley, L.D., Pérez-Suárez, D., de Val-Borro, M., Aldcroft, T.L., Cruz, K.L., Robitaille, T.P., Tollerud, E.J., Ardelean, C., Babej, T., Bach, Y.P., Bachtetti, M., Bakanov, A.V., Bamford, S.P., Barentsen, G., Barmby, P., Baumbach, A., Berry, K.L., Biscani, F., Boquien, M., Bostroem, K.A., Bouma, L.G., Brammer, G.B., Bray, E.M., Breytenbach, H., Buddelmeijer, H., Burke, D.J., Calderone, G., Cano Rodríguez, J.L., Cara, M., Cardoso, J.V.M., Cheelidella, S., Copin, Y., Corrales, L., Crichton, D., D'Avella, D., Deil, C., Depagne, E., Dietrich, J.P., Donath, A., Droettboom, M., Earl, N., Erben, T., Fabbro, S., Ferreira, L.A., Finethy, T., Fox, R.T., Garrison, L.H., Gibbons, S.L.J., Goldstein, D.A., Gommers, R., Greco, J.P., Greenfield, P., Groener, A.M., Grollier, F., Hagen, A., Hirst, P., Homeier, D., Horton, A.J., Hosseinzadeh, G., Hu, L., Hunkeler, J.S., Ivezić, Ž., Jain, A., Jenness, T., Kanarek, G., Kendrew, S., Kern, N.S., Kerzendorf, W.E., Khvalko, A., King, J., Kirkby, D., Kulkarni, A.M., Kumar, A., Lee, A., Lenz, D., Littlefair, S.P., Ma, Z., Macleod, D.M., Mastropietro, M., McCully, C., Montagnac, S., Morris, B.M., Mueller, M., Mumford, S.J., Muna, D., Murphy, N.A., Nelson, S., Nguyen, G.H., Ninan, J.P., Nöthe, M., Ogaz, S., Oh, S., Parejko, J.K., Parley, N., Pascual, S., Patil, R., Patil, A.A., Plunkett, A.L., Prochaska, J.X., Rastogi, T., Reddy Janga, V., Sabater, J., Sakurikar, P., Seifert, M., Sherbert, L.E., Sherwood-Taylor, H., Shih, A.Y., Sick, J., Silbiger, M.T., Singanamalla, S., Singer, L.P., Sladen, P.H., Sooley, K.A., Sornarajah, S., Streicher, O., Teuben, P., Thomas, S.W., Tremblay, G.R., Turner, J.E.H., Terrón, V., van Kerkwijk, M.H., de la Vega, A., Watkins, L.L., Weaver, B.A., Whitmore, J.B., Woillez, J., Zabalza, V., Astropy Contributors: 2018, The Astropy Project: Building an Open-science Project and Status of the v2.0 Core Package. *Astron. J.* **156**, 123. DOI. ADS.
- Brosius, J.W., Rabin, D.M., Thomas, R.J., Landi, E.: 2008, Analysis of a Solar Coronal Bright Point Extreme Ultraviolet Spectrum from the EUNIS Sounding Rocket Instrument. *Astrophys. J.* **677**(1), 781. DOI. ADS.
- Buitrago-Casas, J.C., Glesener, L., Christe, S., Krucker, S., Vievering, J., Athiray, P., Musset, S., Davis, L., Courtade, S., Dalton, G., et al.: 2022, On the faintest solar coronal hard x-rays observed with foxsi. *A&A*, *accepted*.
- Cash, W.: 1979, Parameter estimation in astronomy through application of the likelihood ratio. *Astrophys. J.* **228**, 939. DOI. ADS.
- Cheung, M.C.M., Boerner, P., Schrijver, C.J., Testa, P., Chen, F., Peter, H., Malanushenko, A.: 2015, Thermal Diagnostics with the Atmospheric Imaging Assembly on board the Solar Dynamics Observatory: A Validated Method for Differential Emission Measure Inversions. *Astrophys. J.* **807**(2), 143. DOI. ADS.
- Cooper, K., Hannah, I.G., Grefenstette, B.W., Glesener, L., Krucker, S., Hudson, H.S., White, S.M., Smith, D.M.: 2020, NuSTAR Observation of a Minuscule Microflare in a Solar Active Region. *Astrophys. J. Lett.* **893**(2), L40. DOI. ADS.
- Cooper, K., Hannah, I.G., Grefenstette, B.W., Glesener, L., Krucker, S., Hudson, H.S., White, S.M., Smith, D.M., Duncan, J.: 2021, NuSTAR observations of a repeatedly microflaring active region. *Mon. Not. Roy. Astron. Soc.* **507**(3), 3936. DOI. ADS.
- Del Zanna, G.: 2013, The multi-thermal emission in solar active regions. *Astron. Astrophys.* **558**, A73. DOI. ADS.
- Delouille, V., Mampaey, B., Verbeeck, C., de Visscher, R.: 2012, The SPOCA-suite: a software for extraction and tracking of Active Regions and Coronal Holes on EUV images. *arXiv e-prints*, arXiv:1208.1483. ADS.
- Doschek, G.A., Landi, E., Warren, H.P., Harra, L.K.: 2010, Bright Points and Jets in Polar Coronal Holes Observed by the Extreme-Ultraviolet Imaging Spectrometer on Hinode. *Astrophys. J.* **710**(2), 1806. DOI. ADS.
- Duncan, J., Glesener, L., Grefenstette, B.W., Vievering, J., Hannah, I.G., Smith, D.M., Krucker, S., White, S.M., Hudson, H.: 2021, NuSTAR Observation of Energy Release in 11 Solar Microflares. *Astrophys. J.* **908**(1), 29. DOI. ADS.
- Gehrels, N.: 1986, Confidence Limits for Small Numbers of Events in Astrophysical Data. *Astrophys. J.* **303**, 336. DOI. ADS.

- Glesener, L., Krucker, S., Hannah, I.G., Hudson, H., Grefenstette, B.W., White, S.M., Smith, D.M., Marsh, A.J.: 2017, NuSTAR Hard X-Ray Observation of a Sub-A Class Solar Flare. *Astrophys. J.* **845**(2), 122. DOI. ADS.
- Glesener, L., Krucker, S., Duncan, J., Hannah, I.G., Grefenstette, B.W., Chen, B., Smith, D.M., White, S.M., Hudson, H.: 2020, Accelerated Electrons Observed Down to ~ 7 keV in a NuSTAR Solar Microflare. *Astrophys. J. Lett.* **891**(2), L34. DOI. ADS.
- Golub, L., Krieger, A.S., Silk, J.K., Timothy, A.F., Vaiana, G.S.: 1974, Solar X-Ray Bright Points. *Astrophys. J. Lett.* **189**, L93. DOI. ADS.
- Grefenstette, B.W., Glesener, L., Krucker, S., Hudson, H., Hannah, I.G., Smith, D.M., Vogel, J.K., White, S.M., Madsen, K.K., Marsh, A.J., Caspi, A., Chen, B., Shih, A., Kuhar, M., Boggs, S.E., Christensen, F.E., Craig, W.W., Forster, K., Hailey, C.J., Harrison, F.A., Miyasaka, H., Stern, D., Zhang, W.W.: 2016, The First Focused Hard X-ray Images of the Sun with NuSTAR. *Astrophys. J.* **826**(1), 20. DOI. ADS.
- Hannah, I.G., Kontar, E.P.: 2012, Differential emission measures from the regularized inversion of Hinode and SDO data. *Astron. Astrophys.* **539**, A146. DOI. ADS.
- Hannah, I.G., Hurford, G.J., Hudson, H.S., Lin, R.P., van Bibber, K.: 2007, First Limits on the 3-200 keV X-Ray Spectrum of the Quiet Sun Using RHESSI. *Astrophys. J. Lett.* **659**(1), L77. DOI. ADS.
- Hannah, I.G., Christe, S., Krucker, S., Hurford, G.J., Hudson, H.S., Lin, R.P.: 2008, RHESSI Microflare Statistics. II. X-Ray Imaging, Spectroscopy, and Energy Distributions. *Astrophys. J.* **677**(1), 704. DOI. ADS.
- Hannah, I.G., Hudson, H.S., Hurford, G.J., Lin, R.P.: 2010, Constraining the Hard X-ray Properties of the Quiet Sun with New RHESSI Observations. *Astrophys. J.* **724**(1), 487. DOI. ADS.
- Hannah, I.G., Kleint, L., Krucker, S., Grefenstette, B.W., Glesener, L., Hudson, H.S., White, S.M., Smith, D.M.: 2019, Joint X-Ray, EUV, and UV Observations of a Small Microflare. *Astrophys. J.* **881**(2), 109. DOI. ADS.
- Harrison, F.A., Craig, W.W., Christensen, F.E., Hailey, C.J., Zhang, W.W., Boggs, S.E., Stern, D., Cook, W.R., Forster, K., Giommi, P., Grefenstette, B.W., Kim, Y., Kitaguchi, T., Koglin, J.E., Madsen, K.K., Mao, P.H., Miyasaka, H., Mori, K., Perri, M., Pivovarov, M.J., Puccetti, S., Rana, V.R., Westergaard, N.J., Willis, J., Zoglauer, A., An, H., Bachetti, M., Barrière, N.M., Bellm, E.C., Bhalerao, V., Brejnholt, N.F., Fuerst, F., Liebe, C.C., Markwardt, C.B., Nynka, M., Vogel, J.K., Walton, D.J., Wik, D.R., Alexander, D.M., Cominsky, L.R., Hornschemeier, A.E., Hornstrup, A., Kaspi, V.M., Madejski, G.M., Matt, G., Molendi, S., Smith, D.M., Tomsick, J.A., Ajello, M., Ballantyne, D.R., Baloković, M., Barret, D., Bauer, F.E., Blandford, R.D., Brandt, W.N., Brenneman, L.W., Chiang, J., Chakrabarty, D., Chenevez, J., Comastri, A., Dufour, F., Elvis, M., Fabian, A.C., Farrah, D., Fryer, C.L., Gotthelf, E.V., Grindlay, J.E., Helfand, D.J., Krivonos, R., Meier, D.L., Miller, J.M., Natalucci, L., Ogle, P., Ofek, E.O., Ptak, A., Reynolds, S.P., Rigby, J.R., Tagliaferri, G., Thorsett, S.E., Treister, E., Urry, C.M.: 2013, The Nuclear Spectroscopic Telescope Array (NuSTAR) High-energy X-Ray Mission. *Astrophys. J.* **770**(2), 103. DOI. ADS.
- Harvey, K.L., Strong, K.T., Nitta, N., Tsuneta, S.: 1993, Lifetimes and distribution of coronal bright points observed with Yohkoh. *Advances in Space Research* **13**(9), 27. DOI. ADS.
- Kariyappa, R., Deluca, E.E., Saar, S.H., Golub, L., Damé, L., Pevtsov, A.A., Varghese, B.A.: 2011, Temperature variability in X-ray bright points observed with Hinode/XRT. *Astron. Astrophys.* **526**, A78. DOI. ADS.
- Kontogiannis, I., Tsiropoula, G., Tziotziou, K., Gontikakis, C., Kuckein, C., Verma, M., Denker, C.: 2020, Emergence of small-scale magnetic flux in the quiet Sun. *Astron. Astrophys.* **633**, A67. DOI. ADS.
- Kosugi, T., Matsuzaki, K., Sakao, T., Shimizu, T., Sone, Y., Tachikawa, S., Hashimoto, T., Minesugi, K., Ohnishi, A., Yamada, T., Tsuneta, S., Hara, H., Ichimoto, K., Suematsu, Y., Shimojo, M., Watanabe, T., Shimada, S., Davis, J.M., Hill, L.D., Owens, J.K., Title, A.M., Culhane, J.L., Harra, L.K., Doschek, G.A., Golub, L.: 2007, The Hinode (Solar-B) Mission: An Overview. *Solar Phys.* **243**(1), 3. DOI. ADS.
- Kuhar, M., *et al.*: 2017, Evidence of Significant Energy Input in the Late Phase of a Solar Flare from NuSTAR X-Ray Observations. *Astrophys. J.* **835**(1), 6. DOI. ADS.
- Lemen, J.R., Title, A.M., Akin, D.J., Boerner, P.F., Chou, C., Drake, J.F., Duncan, D.W., Edwards, C.G., Friedlaender, F.M., Heyman, G.F., Hurlburt, N.E., Katz, N.L., Kushner, G.D., Levay, M., Lindgren, R.W., Mathur, D.P., McFeaters, E.L., Mitchell, S., Rehse, R.A., Schrijver, C.J., Springer, L.A., Stern, R.A., Tarbell, T.D., Wuelser, J.-P., Wolfson,

- C.J., Yanari, C., Bookbinder, J.A., Cheimets, P.N., Caldwell, D., Deluca, E.E., Gates, R., Golub, L., Park, S., Podgorski, W.A., Bush, R.I., Scherrer, P.H., Gummin, M.A., Smith, P., Auken, G., Jerram, P., Pool, P., Souffi, R., Windt, D.L., Beardsley, S., Clapp, M., Lang, J., Waltham, N.: 2012, The Atmospheric Imaging Assembly (AIA) on the Solar Dynamics Observatory (SDO). *Solar Phys.* **275**(1-2), 17. DOI. ADS.
- Lin, R.P., Dennis, B.R., Hurford, G.J., Smith, D.M., Zehnder, A., Harvey, P.R., Curtis, D.W., Pankow, D., Turin, P., Bester, M., Csillaghy, A., Lewis, M., Madden, N., van Beek, H.F., Appleby, M., Raudorf, T., McTiernan, J., Ramaty, R., Schmahl, E., Schwartz, R., Krucker, S., Abiad, R., Quinn, T., Berg, P., Hashii, M., Sterling, R., Jackson, R., Pratt, R., Campbell, R.D., Malone, D., Landis, D., Barrington-Leigh, C.P., Slassi-Sennou, S., Cork, C., Clark, D., Amato, D., Orwig, L., Boyle, R., Banks, I.S., Shirey, K., Tolbert, A.K., Zarro, D., Snow, F., Thomsen, K., Henneck, R., McHedlishvili, A., Ming, P., Fivian, M., Jordan, J., Wanner, R., Crubb, J., Preble, J., Matraga, M., Benz, A., Hudson, H., Canfield, R.C., Holman, G.D., Crannell, C., Kosugi, T., Emslie, A.G., Vilmer, N., Brown, J.C., Johns-Krull, C., Aschwanden, M., Metcalf, T., Conway, A.: 2002, The Reuven Ramaty High-Energy Solar Spectroscopic Imager (RHESSI). *Solar Phys.* **210**(1), 3. DOI. ADS.
- Madjarska, M.S.: 2019, Coronal bright points. *Living Reviews in Solar Physics* **16**(1), 2. DOI. ADS.
- Madsen, K.K., Forster, K., Grefenstette, B.W., Harrison, F.A., Miyasaka, H.: 2021, 2021 Effective Area calibration of the Nuclear Spectroscopic Telescope ARray (NuSTAR). *arXiv e-prints*, arXiv:2110.11522. ADS.
- Mou, C., Madjarska, M.S., Galsgaard, K., Xia, L.: 2018, Eruptions from quiet Sun coronal bright points. I. Observations. *Astron. Astrophys.* **619**, A55. DOI. ADS.
- Parker, E.N.: 1988, Nanoflares and the Solar X-Ray Corona. *Astrophys. J.* **330**, 474. DOI. ADS.
- Reale, F., McTiernan, J.M., Testa, P.: 2009, Comparison of Hinode/XRT and RHESSI Detection of Hot Plasma in the Non-Flaring Solar Corona. *Astrophys. J. Lett.* **704**(1), L58. DOI. ADS.
- Schmelz, J.T., Kashyap, V.L., Saar, S.H., Dennis, B.R., Grigis, P.C., Lin, L., De Luca, E.E., Holman, G.D., Golub, L., Weber, M.A.: 2009, Some Like It Hot: Coronal Heating Observations from Hinode X-ray Telescope and RHESSI. *Astrophys. J.* **704**(1), 863. DOI. ADS.
- Schmelz, J.T., Asgari-Targhi, M., Christian, G.M., Dhaliwal, R.S., Pathak, S.: 2015, Hot Plasma from Solar Active Region Cores: a Test of AC and DC Coronal Heating Models? *Astrophys. J.* **806**(2), 232. DOI. ADS.
- Shimojo, M., Shibata, K.: 1999, Occurrence Rate of Microflares in an X-Ray-bright Point within an Active Region. *Astrophys. J.* **516**(2), 934. DOI. ADS.
- SunPy Community, T., Mumford, S.J., Christe, S., Pérez-Suárez, D., Ireland, J., Shih, A.Y., Inglis, A.R., Liedtke, S., Hewett, R.J., Mayer, F., Hughitt, K., Freij, N., Meszaros, T., Bennett, S.M., Malocha, M., Evans, J., Agrawal, A., Leonard, A.J., Robitaille, T.P., Mampaey, B., Iván Campos-Rozo, J., Kirk, M.S.: 2015, SunPy—Python for solar physics. *Computational Science and Discovery* **8**(1), 014009. DOI. ADS.
- Testa, P., Reale, F., Landi, E., DeLuca, E.E., Kashyap, V.: 2011, Temperature Distribution of a Non-flaring Active Region from Simultaneous Hinode XRT and EIS Observations. *Astrophys. J.* **728**(1), 30. DOI. ADS.
- van Driel-Gesztelyi, L., Green, L.M.: 2015, Evolution of Active Regions. *Living Reviews in Solar Physics* **12**(1), 1. DOI. ADS.
- Wright, P.J., Hannah, I.G., Grefenstette, B.W., Glesener, L., Krucker, S., Hudson, H.S., Smith, D.M., Marsh, A.J., White, S.M., Kuhar, M.: 2017, Microflare Heating of a Solar Active Region Observed with NuSTAR, Hinode/XRT, and SDO/AIA. *Astrophys. J.* **844**(2), 132. DOI. ADS.
- Zhang, J., Kundu, M.R., White, S.M.: 2001, Spatial Distribution and Temporal Evolution of Coronal Bright Points. *Solar Phys.* **198**(2), 347. DOI. ADS.